

Predicting reliable H₂ column density maps from molecular line data using machine learning

Yoshito SHIMAJIRI,^{1*} Yasutomo KAWANISHI,² Shinji FUJITA,^{3,4} Yusuke MIYAMOTO,⁵ Atsushi M. ITO,⁶ Doris ARZOUMANIAN,⁷ Philippe ANDRÉ,⁸ Atsushi NISHIMURA,⁷ Kazuki TOKUDA,^{4,7,9} Hiroyuki KANEKO, Shunya TAKEKAWA,¹¹ Shota UEDA,⁴ Toshikazu ONISHI,⁴ Tsuyoshi INOUE,¹² Shimpei NISHIMOTO,⁴ and Ryuki YONEDA⁴

¹ Kyushu Kyoritsu University, Jiyugaoka 1-8, Yahatanishi-ku, Kitakyushu, Fukuoka, 807-08585, Japan

² RIKEN Information R&D and Strategy Headquarters, 2-2-2 Hikaridai, Seika-cho, Soraku-gun, Kyoto, 619-0288, Japan

³ Institute of Astronomy, Graduate School of Science, The University of Tokyo, 2-21-1 Osawa, Mitaka, Tokyo 181-0015, Japan

⁴ Department of Physics, Graduate School of Science, Osaka Metropolitan University, 1-1 Gakuen-cho, Naka-ku, Sakai, Osaka 599-8531, Japan

⁵ Department of Electrical and Electronic Engineering, Fukui University of Technology, 3-6-1, Gakuen, Fukui, 910-8505, Japan

⁶ National Institute for Fusion Science (NIFS), National Institutes of Natural Sciences (NINS), 322-6, Oroshi-cho, Toki, Gifu, 509-5292, Japan

⁷ National Astronomical Observatory of Japan, Osawa 2-21-1, Mitaka, Tokyo, 181-8588, Japan

⁸ Laboratoire d'Astrophysique (AIM), Université Paris-Saclay, Université Paris Cité, CEA, CNRS, AIM, 91191 Gif-sur-Yvette, France

⁹ Department of Earth and Planetary Sciences, Faculty of Science, Kyushu University, Nishi-ku, Fukuoka 819-0395, Japan

¹⁰ Graduate School of Education, Joetsu University of Education, 1, Yamayashiki-machi, Joetsu, Niigata 943-8512, Japan

¹¹ Department of Applied Physics, Faculty of Engineering, Kanagawa University, 3-27-1 Rokkakubashi, Kanagawa-ku, Yokohama, Kanagawa, 221-8686, Japan

¹² Department of Physics, Konan University, 8-9-1 Okamoto, Higashinada-ku, Kobe, Hyogo, 658-8501, Japan

Accepted XXX. Received YYY; in original form ZZZ

ABSTRACT

The total mass estimate of molecular clouds suffers from the uncertainty in the H₂-CO conversion factor, the so-called X_{CO} factor, which is used to convert the ¹²CO (1–0) integrated intensity to the H₂ column density. We demonstrate the machine learning's ability to predict the H₂ column density from the ¹²CO, ¹³CO, and C¹⁸O (1–0) data set of four star-forming molecular clouds; Orion A, Orion B, Aquila, and M17. When the training is performed on a subset of each cloud, the overall distribution of the predicted column density is consistent with that of the *Herschel* column density. The total column density predicted and observed is consistent within 10%, suggesting that the machine learning prediction provides a reasonable total mass estimate of each cloud. However, the distribution of the column density for values $> \sim 2 \times 10^{22} \text{ cm}^{-2}$, which corresponds to the dense gas, could not be predicted well. This indicates that molecular line observations tracing the dense gas are required for the training. We also found a significant difference between the predicted and observed column density when we created the model after training the data on different clouds. This highlights the presence of different X_{CO} factors between the clouds, and further training in various clouds is required to correct for these variations. We also demonstrated that this method could predict the column density toward the area not observed by *Herschel* if the molecular line and column density maps are available for the small portion, and the molecular line data are available for the larger areas.

Key words: ISM: clouds – ISM: molecules – ISM: abundances – methods: statistical

1 INTRODUCTION

In astronomy, especially in studies of the interstellar medium (ISM), it is essential to investigate the spatial distribution and mass of molecular hydrogen, H₂, since molecular hydrogen is the most abundant molecule in the universe. Since it is difficult to directly observe the H₂ emission in the cold (~ 10 –20K) ISM, the ¹²CO (1–0) emission is instead used to measure the mass of the molecular gas by using the relation between the ¹²CO integrated intensity and the H₂ column density of $N(\text{H}_2)[\text{cm}^{-2}] = X_{\text{CO}}[\text{cm}^{-2}/\text{K km s}^{-1}] \times W(^{12}\text{CO})[\text{K km s}^{-1}]$ where $N(\text{H}_2)$, $W(^{12}\text{CO})$, and X_{CO} are the H₂ column density, the

integrated intensity of ¹²CO (1–0), and H₂-to-CO conversion factor, respectively. Bolatto et al. (2013) found a conversion factor of $X_{\text{CO}} = 2 \times 10^{20} [\text{cm}^{-2}/\text{K km s}^{-1}]$ with $\pm 30\%$ uncertainty in the Milky Way. The column density is also derived from the molecular line data assuming the local thermodynamic equilibrium (LTE) condition by the following equation (e.g., Mangum & Shirley 2015).

$$N_{\text{mol}} = \frac{3h}{8\pi^3} \frac{Q}{\mu S_{i,j}} \frac{e^{E_u/kT_{\text{ex}}}}{e^{h\nu/kT_{\text{ex}}} - 1} \int \tau d\nu \quad (1)$$

where k , h , ν , Q , μ , E_u , $S_{i,j}$, and τ are the Boltzmann constant, the Planck constant, the rest frequency of the molecular line, the partition function, the dipole moment, the energy of the upper level, and the

* E-mail: y-shimajiri@fains.jp

Table 1. Data-set

Cloud	Orion A	Orion B/NGC 2024	Aquila	M 17
$^{12}\text{CO}(1-0)^\dagger$	Shimajiri et al. (2011); Nakamura et al. (2019)	Shimajiri et al. (2023)	Shimoikura et al. (2019a)	Shimoikura et al. (2019b); Sugitani et al. (2019)
$^{13}\text{CO}(1-0)^\dagger$	Shimajiri et al. (2011, 2014)	Shimajiri et al. (2023)	Shimoikura et al. (2019a)	Shimoikura et al. (2019b); Sugitani et al. (2019)
$\text{C}^{18}\text{O}(1-0)^\dagger$	Shimajiri et al. (2011, 2014)	Shimajiri et al. (2023)	Shimoikura et al. (2019a)	Shimoikura et al. (2019b); Sugitani et al. (2019)
$N_{\text{H}_2}^\ddagger$	André et al. (2010) [‡] ; Pezzuto et al. in prep.	Könyves et al. (2020) [‡]	Könyves et al. (2015) [‡]	Motte et al. (2010) [♣]

[[†]] $^{12}\text{CO}(1-0)$, $^{13}\text{CO}(1-0)$, and $\text{C}^{18}\text{O}(1-0)$ data are obtained with the Nobeyama 45m. The column density N_{H_2} is derived from *Herschel* data.

[[‡]] HGBS Archive (<http://gouldbelt-herschel.cea.fr/archives>).

[[♣]] HOBYS Archive (<http://hobys-herschel.cea.fr>).

intrinsic line strength of the transition for i to j state, and the optical depth. T_{ex} is the excitation temperature which can be derived from $^{12}\text{CO}(1-0)$ as follows (c.f., Nishimura et al. 2015):

$$T_{\text{ex}} = 5.53 \left\{ \ln \left[1 + \frac{5.53}{T_{\text{peak}} + 0.84} \right] \right\}^{-1} \quad (2)$$

where T_{peak} is the peak intensity of $^{12}\text{CO}(1-0)$. To convert the N_{mol} to H_2 column density $N(\text{H}_2)$, the molecular abundance X_{mol} is also required (i.e., $N(\text{H}_2) = N_{\text{mol}}/X_{\text{mol}}$). However, molecular abundance is known to have a large variation on a wide scale range from the core scale to the scale of a galaxy (c.f. Watanabe et al. 2014; Shimajiri et al. 2015b; Nishimura et al. 2016; Shimajiri et al. 2017; Watanabe et al. 2019; Tokuda et al. 2021). Furthermore, the abundance ratios between ^{13}CO and C^{18}O and between ^{12}CO and ^{13}CO change due to the selective FUV (far ultraviolet) dissociation, suggesting that these abundances vary with the FUV radiation (Shimajiri et al. 2014; Nishimura et al. 2015; Lin et al. 2016; Ishii et al. 2019). The FUV radiation changes the molecular abundance in the ISM. Thus, adopting the appropriate molecular abundance and taking into account the FUV radiation effect are crucial to derive the H_2 column density accurately.

As mentioned above, the mass estimate has a large uncertainty despite its importance in describing the physical properties of molecular clouds. The amount of information increases rapidly with the advent of astronomical instruments. Recently, machine learning methods have been applied to various astronomical data sets for diverse scientific objectives such as the classification of galaxies (Barchi et al. 2020), clustering into exoplanets (Schanche et al. 2019), identification of the ring structures surrounding the HII region (Ueda et al. 2020; Nishimoto et al. 2022), solving Near and far problem in inner Galaxy (Fujita et al. 2022), identifying the filamentary structure (Zavagno et al. 2023) and so on. Gratier et al. (2021) demonstrated that the H_2 column density could be predicted from multi-molecular line emission using one of the machine-learning methods, the *random forest*. They used multi-molecular line data toward Orion B obtained with the IRAM30m telescope. They found that the ^{12}CO , ^{13}CO , and C^{18}O lines play significant roles in predicting the H_2 column density. For higher-density areas, the dense gas tracers such as HNC, HCO^+ , and N_2H^+ are also important.

This study uses the machine learning technique to predict the H_2 column density from the combined analysis of the ^{12}CO , ^{13}CO , and C^{18}O data sets. The ^{12}CO , ^{13}CO , and C^{18}O emissions are frequently used to derive the mass of the ISM and to trace the cloud structures well. With the advent of new receivers and correlators (such as those on the Nobeyama 45m telescope), it is feasible to observe these lines simultaneously. Furthermore, the intensities of these lines are stronger than those of the dense gas tracers such as H^{13}CO^+ , and N_2H^+ . Consequently, wide-field mapping of molecular clouds is possible with these three CO isotopologues. In fact, many surveys

toward star forming regions in ^{12}CO , ^{13}CO , and C^{18}O have been conducted (Umemoto et al. 2017; Braiding et al. 2018; Nakamura et al. 2019; Su et al. 2019; Torii et al. 2019). Thus, revealing how accurately the structure and mass of molecular clouds can be reconstructed from the ^{12}CO , ^{13}CO , and C^{18}O using machine learning will provide new tools to study the ISM physics and star formation. This paper is organized as follows: In Sect. 2, we describe the data set used in the paper. In Sect. 3, we described the data preprocessing, optimization setup, training, and test. In Sect. 4, we show the results derived from applying the model produced by the Extra Trees Regressor (ET, Geurts et al. 2006). In Sect. 5, we will evaluate the accuracy of column density predictions and predict column densities at higher spatial resolution. Our conclusions are summarized in Sect. 6.

2 DATA SET

Maps of $^{12}\text{CO}(J=1-0)$, $^{13}\text{CO}(J=1-0)$, and $\text{C}^{18}\text{O}(J=1-0)$ toward Orion A, Orion B/NGC 2024, Aquila, and M 17 are publicly available from Shimajiri et al. (2011, 2014); Shimoikura et al. (2019b,a); Sugitani et al. (2019); Nakamura et al. (2019) (see Table 1).

In parallel, good H_2 column density maps of the same regions derived from *Herschel* submillimeter dust continuum data are available (see Table 1, André et al. 2010; Motte et al. 2010; Könyves et al. 2015, 2020, Pezzuto et al. in prep.).

The ^{12}CO , ^{13}CO , and C^{18}O data were obtained with the Nobeyama 45m telescope. The angular resolution of the data used in this study is $25''$ smoothed from the original effective angular resolution of $20-21''$ to improve the sensitivity. The integrated intensity and peak intensity maps are then produced from these cube data. The integrated intensity ratios of ^{12}CO to ^{13}CO and of ^{13}CO to C^{18}O are also produced (see Fig. 1).

The reference H_2 column density maps we use in this paper have an angular resolution of $18.2''$ and were derived from *Herschel* Gould Belt Survey (HGBS) data (André et al. 2010) and *Herschel* imaging survey of OB Young Stellar objects (HOBYS) data (Motte et al. 2010) by fitting the observed spectral energy distributions (SEDs) between 160 and 500 microns on a pixel-by-pixel basis and employing the multi-resolution procedure described in Appendix A of Palmeirim et al. (2013). Since submillimeter dust continuum emission is optically thin and has a wide density dynamic range, it thus traces reliably the wide range of densities present in molecular clouds. The angular resolution of the H_2 column density is smoothed from the original angular resolution of $18''.2$ to $25''$ to be the same as that of the molecular line data. The uncertainty of the H_2 column density derived from the HGBS data is a factor of 2 (Roy et al. 2014).

The maps of ^{12}CO , ^{13}CO , and C^{18}O are made with a pixel size of $7''.5$. The HGBS H_2 column density maps were regrid to align to the same grid as the molecular line data.

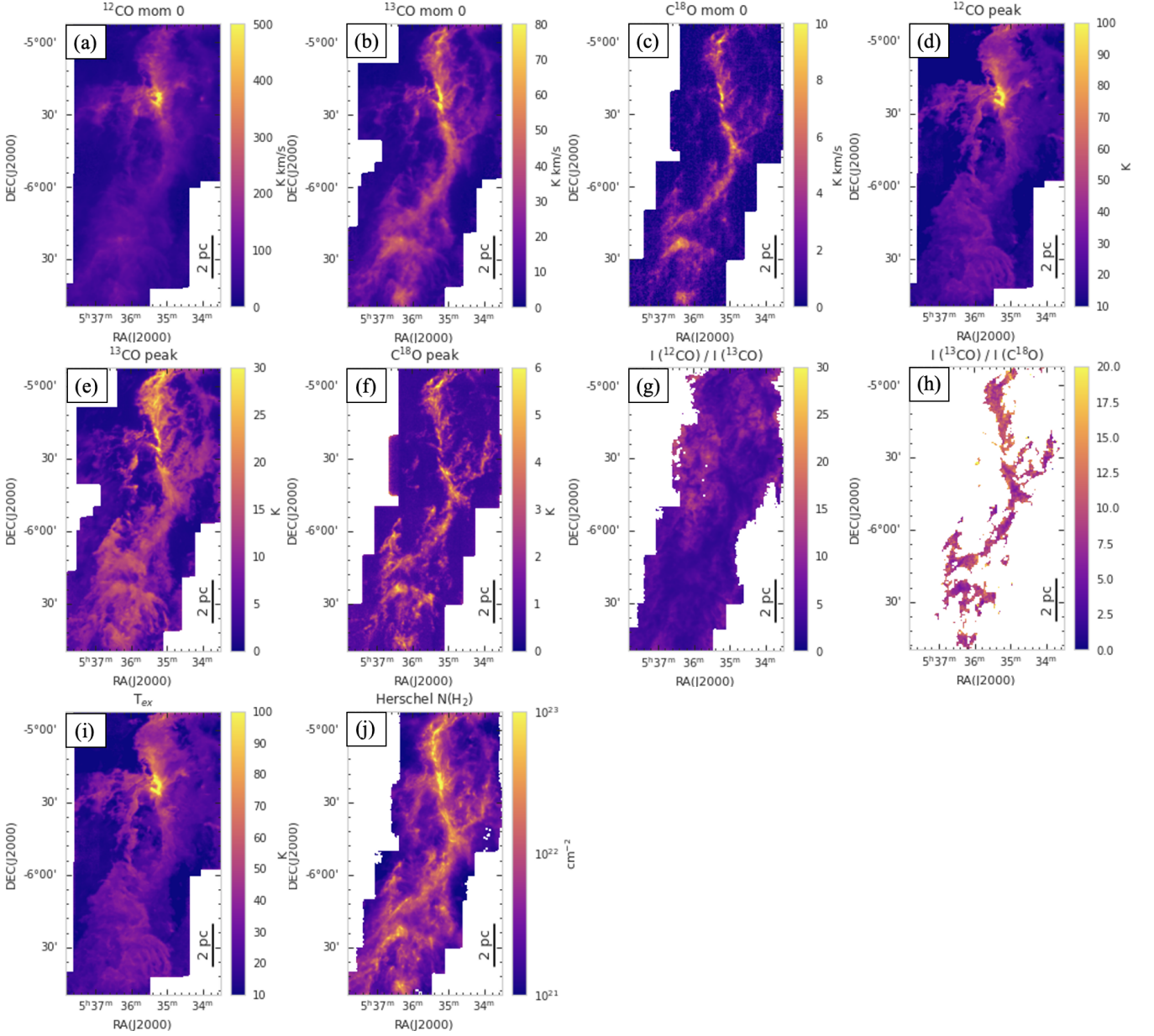


Figure 1. (a – c) ^{12}CO (1–0), ^{13}CO (1–0), and C^{18}O (1–0) integrated intensity (moment 0) maps, (d – f) ^{12}CO , ^{13}CO , and C^{18}O peak intensity maps, (g – h) maps of the integrated intensity ratio of ^{12}CO to ^{13}CO and of ^{13}CO to C^{18}O , (i) excitation temperature map, and (j) HGBS H_2 column density map toward Orion A molecular cloud. The angular resolution of all maps is smooth to $25''$.

Table 2. Example of the list used as input for the training

RA _{pix}	DEC _{pix}	^{12}CO Mom 0 [K km/s]	^{13}CO Mom 0 [K km/s]	C^{18}O Mom 0 [K km/s]	^{12}CO Peak [K]	^{13}CO Peak [K]	C^{18}O Peak [K]	T_{ex} [K]	$\frac{^{12}\text{CO mom0}}{^{13}\text{CO mom0}}$	$\frac{^{13}\text{CO mom0}}{\text{C}^{18}\text{O mom0}}$	$N(\text{H}_2)$ [$\times 10^{21}\text{cm}^{-2}$]	cloud	
383	145	245	46.027042	13.917648	1.410226	17.584301	7.415209	1.891411	21.047360	3.307099	9.869093	5.025195	orion
432	146	205	53.787624	14.213110	0.627789	13.870554	8.023403	2.044455	17.307561	3.784367	22.639942	8.674680	orion
433	146	206	55.570644	15.812763	0.706174	14.270488	7.973323	2.304390	17.710831	3.514291	22.392151	10.559992	orion
437	146	210	62.206879	20.084249	0.945845	15.013415	9.388056	1.692411	18.459568	3.097297	21.234194	12.494176	orion
438	146	211	63.578884	20.229988	0.972942	15.296682	9.360451	2.014358	18.744927	3.142804	20.792583	12.344450	orion
...

Example of the list used as input for the training with from left to right, a pixel running number, the coordinates in pixel, the integrated intensity, peak intensity, of ^{12}CO , ^{13}CO , and C^{18}O , the ratio of ^{12}CO to ^{13}CO , the ratio of ^{13}CO to C^{18}O , the excitation temperature, the HGBS H_2 column density, and the cloud name.

Table 3. Tuned hyperparameters for each data-set

Regressor	Regressor- OMC1	Regressor- OMC123	Regressor- NGC2024	Regressor- Aquila	Regressor- M17	Regressor- High-Resolution
area used for training	Orion A/ OMC-1	Orion A/ OMC-1/2/3	Orion B/ NGC 2024	Aquila	M 17	Orion A OMC-1/2/3
blc_RA [†]	5 ^h 36 ^m 8 ^s .8	5 ^h 36 ^m 8 ^s .8	5 ^h 42 ^m 14 ^s .7	18 ^h 31 ^m 43 ^s .1	0 ^h 57 ^m 22 ^s .0	5 ^h 5 ^m 47 ^s .4
blc_DEC [†]	-5 ^d 29 ^m 43 ^s .7	5 ^d 33 ^m 28 ^s .7	-1 ^d 58 ^m 5 ^s .9	-2 ^d 12 ^m 29 ^s .0	0 ^d 36 ^m 45 ^s .0	-5 ^d 29 ^m 44 ^s .9
trc_RA [‡]	5 ^h 34 ^m 28 ^s .4	5 ^h 34 ^m 28 ^s .4	5 ^h 41 ^m 27 ^s .2	18 ^h 29 ^m 50 ^s .0	0 ^h 55 ^m 22 ^s .0	5 ^h 34 ^m 42 ^s .3
trc_DEC [‡]	-5 ^d 15 ^m 58 ^s .8	-4 ^d 55 ^m 58 ^s .8	-1 ^d 54 ^m 58 ^s .4	-1 ^d 58 ^m 44 ^s .2	0 ^d 26 ^m 44 ^s .9	-4 ^d 57 ^m 24 ^s .8
number of samples (pixels) in training set	22311	60501	2496	25197	19521	472269
number of samples (pixels) in the area observed in CO/ ¹³ CO/C ¹⁸ O	330030	330030	25124	131040	106328	5426235
max_depth ¹	11	11	7	11	11	11
max_features ²	1	1	1	1	1	1
min_samples_leaf ³	1	1	2	1	1	1
min_samples_split ⁴	2	2	5	3	3	5
min_weight_fraction_leaf ⁵	0	0	0	0	0	0
n_estimators ⁶	245	300	244	241	256	251

[†]: RA and DEC coordinates of the bottom left corner of the trained area.

[‡]: RA and DEC coordinates of the top right corner of the trained area.

¹:The maximum depth of the tree.

²:The limit of the maximum number of features used for each tree.

³:The minimum number of samples required to be at a leaf node.

⁴:The minimum number of samples required to split an internal node.

⁵:The minimum weighted fraction of the sum total of weights (of all the input samples) required to be at a leaf node.

⁶: The number of trees in the forest.

Table 4. Comparison among models

Model		MAE	MSE	RMSE	R2	RMSLE	MAPE	TT
		<i>Mean Absolute Error</i>	<i>Mean Square Error</i>	<i>Root Mean Square Error</i>	<i>R-Squared</i>	<i>Root Mean Square Error</i>	<i>Mean Absolute Percentage Error</i>	<i>Training Time</i>
		[$\times 10^{21}$ cm ⁻²]		[$\times 10^{21}$ cm ⁻²]			[%]	[sec]
et	Extra Trees Regressor	2.3205	92.2658	8.8934	0.9020	0.1680	0.1451	0.962
lightgbm	Light Gradient Boosting Machine	3.2010	213.8056	13.0801	0.8457	0.2102	0.1899	0.599
rf	Random Forest Regressor	2.7379	151.9937	11.2724	0.8166	0.1827	0.1571	0.872
gbr	Gradient Boosting Regressor	3.3099	160.4642	12.0486	0.8001	0.2365	0.2304	0.567
ada	AdaBoost Regressor	10.0274	287.9909	16.4738	0.6675	0.8676	1.7285	0.188
knn	K Neighbors Regressor	4.8112	420.5454	19.3340	0.6282	0.2777	0.2324	0.135
dt	Decision Tree Regressor	3.6443	316.4728	16.6898	0.5835	0.2528	0.2002	0.028
omp	Orthogonal Matching Pursuit	11.6651	661.4842	24.1136	0.4528	0.7900	1.4896	0.006
lr	Linear Regression	11.9426	801.5580	25.0735	0.3844	0.8129	1.7359	0.005
ridge	Ridge Regression	11.9412	805.8845	25.1101	0.3820	0.8126	1.7356	0.006
br	Bayesian Ridge	11.9338	845.8109	25.4381	0.3597	0.8106	1.7344	0.007
huber	Huber Regressor	6.0315	928.7155	27.9140	0.3125	0.4323	0.4065	0.056
par	Passive Aggressive Regressor	9.6714	1020.8535	29.4623	0.2129	0.6885	0.9275	0.008
llar	Lasso Least Angle Regression	12.0764	1214.2287	32.9040	-0.0066	0.9467	1.6193	0.006
dummy	Dummy Regressor	12.0764	1214.2287	32.9040	-0.0066	0.9467	1.6193	0.003
lasso	Lasso Regression	11.7063	1771.4781	30.7326	-0.1609	0.7718	1.6734	0.009
lar	Least Angle Regression	16.1396	2069.0267	33.7691	-0.4530	1.0109	2.5780	0.007
en	Elastic Net	11.7823	3071.2942	36.0023	-0.9102	0.7729	1.7297	0.008

3 MACHINE LEARNING

3.1 Data preprocessing

The images of the integrated intensity, peak intensity, ratio of ¹²CO to ¹³CO, the ratio of ¹³CO to C¹⁸O, the excitation temperature derived using Eq. (2), and H₂ column density shown in Fig. 1 are

converted into the data frame as listed in Table 2. We made regressors trained on the data set for small portions of the OMC-1, OMC-1/2/3, NGC 2024, Aquila, and M 17 clouds, hereafter referred to as Regressor-OMC1, Regressor-OMC123, Regressor-NGC2024, Regressor-Aquila, and Regressor-M17, respectively. Table 3 lists the

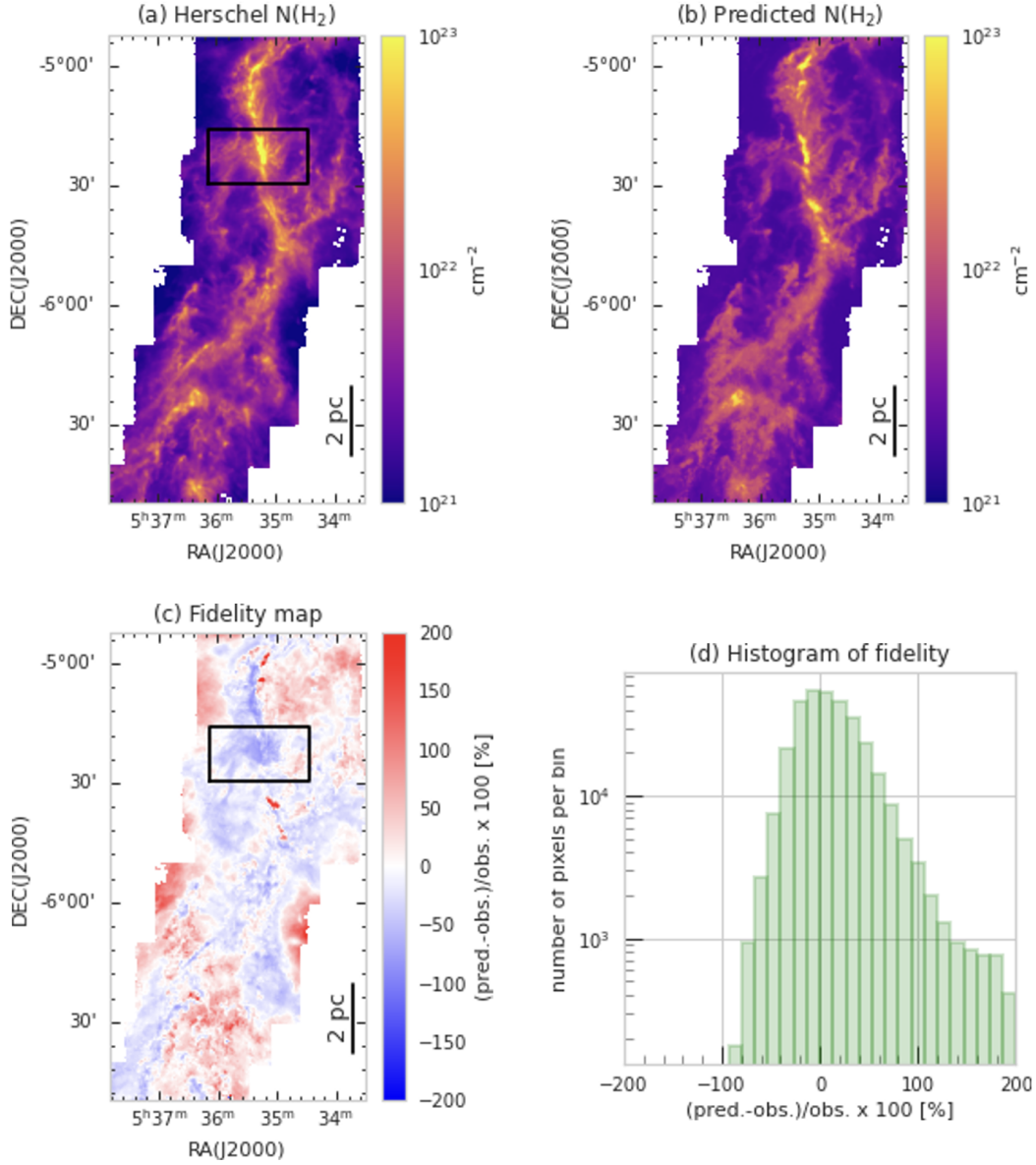


Figure 2. Maps of (a) the HGBS H_2 column density, (b) the H_2 column density predicted by Regressor-OMC1, (c) the fidelity between the observations and the prediction toward Orion A molecular cloud, and (d) histogram of the fidelity. The black box in panels (a) and (c) indicates the area used for training the regressor. In panel (b), the H_2 column density is predicted by Regressor-OMC1 from the molecular line data.

trained area for each regressor. In Figures 2, A1, A2, A3, and A4, the area used for each regressor is indicated by the black box.

3.2 Selection of the regression model

In the python package *pycaret*, the available regression models are Extra Trees Regressor (ET), Random Forest Regressor (RF), Gradient Boosting Regressor (GBR), Decision Tree Regressor (DT), Light Gradient Boosting Machine (LightGBM), K Neighbors Regressor (KNN), AdaBoost Regressor (ADA), Lasso Regression (LASSO), Bayesian Ridge (BR), Linear Regression (LR), Ridge Regression (RIDGE), Elastic Net (EN), Orthogonal Matching Pursuit (OMP), Huber Regressor (HUBER), Least Angle Regression (LAR), Passive Aggressive Regressor (PAR), Lasso Least Angle Regression (LLAR), and Dummy Regressor (DUMMY). To select the best model for this study, we evaluated the performance of these models using a

function *compare_models*. The *compare_models* function trains and evaluates the performance of all available models using the k -fold cross-validation method with the defined fold parameter (default = 10 folds, which was used in this study). The data are divided into k subsets. One data subset is used for the test, while the $k-1$ subsets are used for training. The learning is continued k times to make all k dataset be used for testing. Then, the accuracy averaged over k training sessions is used for evaluation. During the evaluation, the parameters are tuned to minimize the value of RMSLE (Root Mean Square Logarithmic Error). The ET was selected based on the comparison of RMSLE among models. The Extra Trees Regressor generates many decision trees, similar to the Random Forest Regressor (Geurts et al. 2006). Random Forest is one of the most representative methods used in machine learning for classification, regression, and clustering. It takes random samples from the entire data set, allowing for duplicates, and uses these samples to build multiple decision trees. Each

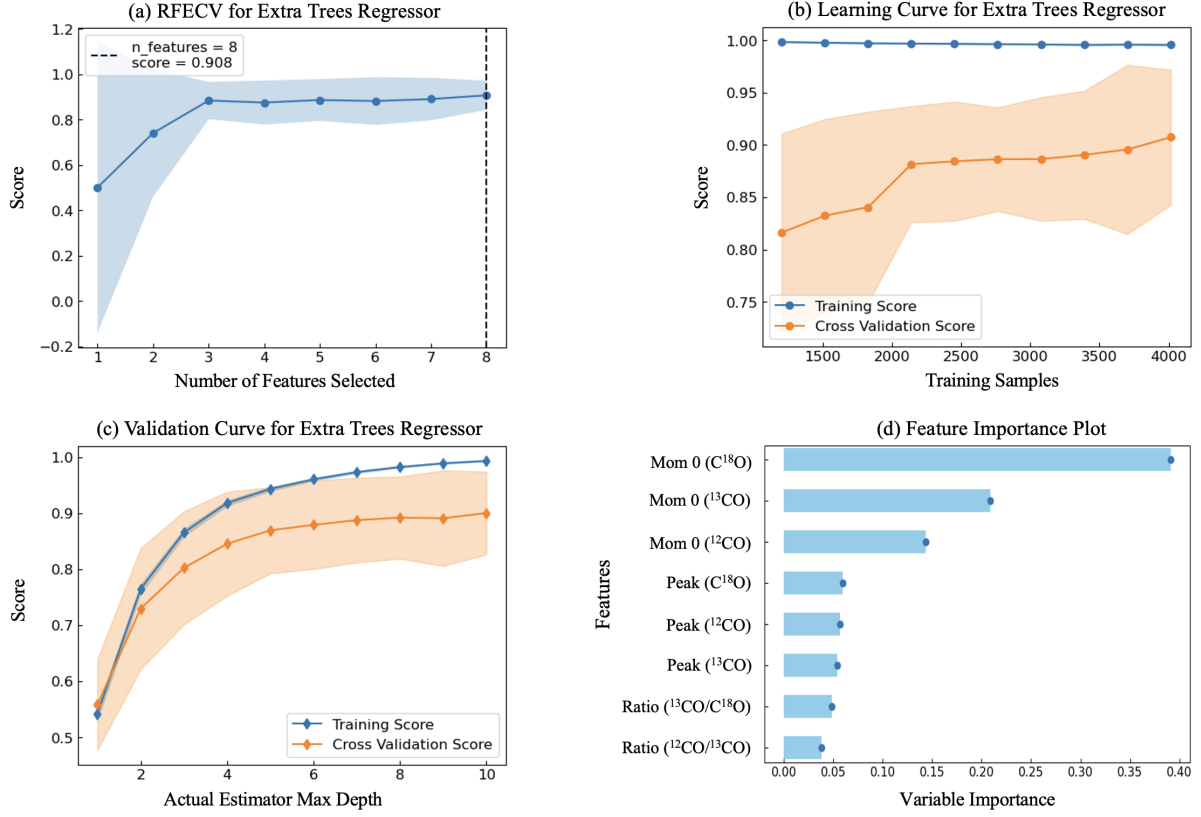


Figure 3. Plots of (a) the recursive feature elimination with the cross-validation (RFECV), (b) learning curve, (c) validation curve, and (d) importance of each feature for Regressor-OMC1. The blue and orange curves indicate the training and cross-validation scores in panels (b) and (c). In panels (a), (b), and (c), the blue and orange filled curves indicate the range of the standard deviation of the score. The score indicates R2.

tree is a hierarchical structure (flowchart-like tree structure) where an internal node represents a feature, the branch represents a decision rule, and each leaf node represents the outcome. Thus, each tree in the random forest is built on a subset sampled from the original data set and therefore has a different trend. In the Extra Trees Regressor, a certain number of features within the entire set are randomly selected for each tree. The Extra Trees Regressor also randomly selects thresholds for each feature. These have the effect of avoiding overfitting. Table 4 shows RMSLE as well as MAE (Mean Absolute Error), MSE (Mean Square Error), RMSE (Root Mean Square Error), R2 (R-Squared), MAPE (Mean Absolute Percentage Error), and Training Time (TT) for each model. The definitions of MAE, MSE, RMSE, R2, RMSLE, and MAPE are given below.

$$\text{MAE} = \frac{1}{n} \sum_{i=1}^n |\hat{y}_i - y_i|, \quad (3)$$

$$\text{MSE} = \frac{1}{n} \sum_{i=1}^n (\hat{y}_i - y_i)^2, \quad (4)$$

$$\text{RMSE} = \sqrt{\frac{1}{n} \sum_{i=1}^n (\hat{y}_i - y_i)^2}, \quad (5)$$

$$\text{R2} = 1 - \frac{\sum_{i=1}^n (\hat{y}_i - y_i)^2}{\sum_{i=1}^n (\bar{y} - y_i)^2}, \quad (6)$$

$$\text{RMSLE} = \sqrt{\frac{1}{n} \sum_{i=1}^n (\log \hat{y}_i - \log y_i)^2}, \quad (7)$$

$$\text{MAPE} = \frac{1}{n} \sum_{i=1}^n \left(\frac{\hat{y}_i - y_i}{y_i} \right)^2, \quad (8)$$

where n , \hat{y}_i , y_i , \bar{y} are the pixel number for each data, the predicted value for i th data, observed value for i th data, and the average of the observed values. These evaluation indexes, except R2, take lower values for better accuracy, while R2 ranges from 0 to 1 and takes values closer to 1 for better accuracy. The model of Extra Trees Regressor (ET) shows the best scores in MAE, MSE, RMSE, RMSLE, and MAPE, except R2 as can be seen in Table 4. We thus use ET in this study.

3.3 Optimization of setup

To tune the hyperparameters of the ET, we used a function `tune_model` in the python package `pycaret`. This function tunes the hyperparameters automatically using the random grid search.

In general, as increasing the number of features, the model becomes more complex and overfitted. Recursive feature elimination (RFE) is one of the methods to avoid overfitting. In this method, first, the model is produced using all features. Then, another model is produced using all features except the feature showing the lowest importance in the previous cycle. These steps are repeated. RFECV

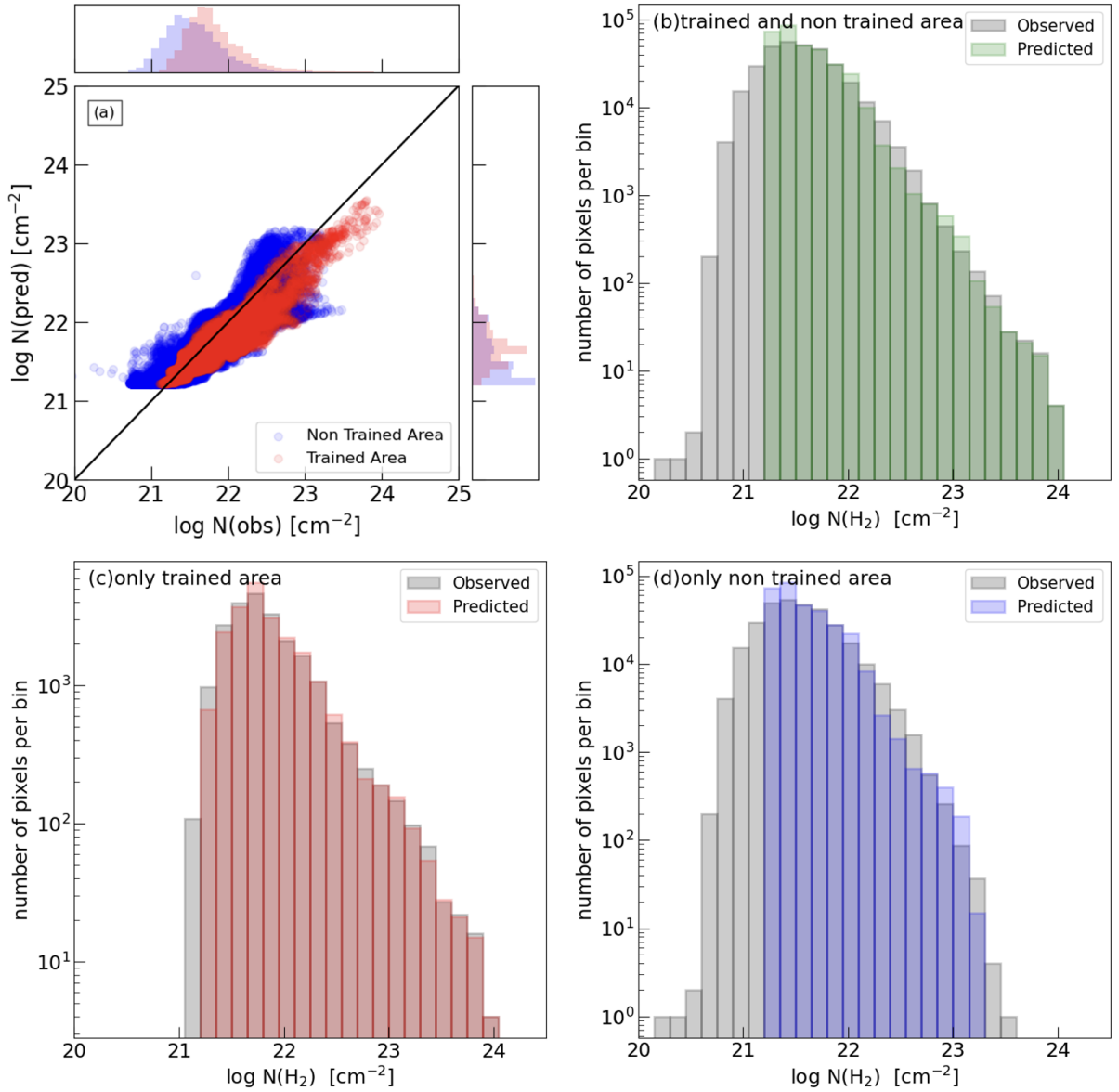


Figure 4. (a) Pixel-to-pixel correlation between predicted and observed H_2 column density and (b) pixel-by-pixel H_2 column density histogram for predicted and observed H_2 column density in the whole Orion A region, (c) pixel-by-pixel H_2 column density histogram for predicted and observed H_2 column density in the area trained for Regressor-OMC1 (i.e., inside of the black box in Fig. 2a), and (d) pixel-by-pixel H_2 column density histogram for predicted and observed H_2 column density in the area not used for Regressor-OMC1 (i.e., outside of the black box in Fig. 2a). In panel (a), the black line indicates the predicted H_2 column density equals the observed H_2 column density. The top and right on the panel (a) show the histograms of $\log N(\text{obs})$ and $\log N(\text{pred})$ for the non-trained area and trained area, respectively. In panel (b-d), the red, green, and blue indicate the predicted H_2 column density, while the gray indicates the observed H_2 column density.

is the method in that recursive feature elimination (RFE) is processed with cross-validation (CV). Figure 3 (a) shows the RFECV plot. The score increases as the number of selected features increases. As a result, eight features are selected for making the model. Figure 3 (b) shows the learning curve. The learning curve shows scores for different numbers of training samples. At the beginning of the training, as updating the training model, the scores increase and the gap between the scores for the training data and test (cross-validation) data becomes small, suggesting the effect of the overfitting is improved. Figure 3 (c) shows the validation curves when the hyperparameter

ter max_depth value changes¹. This parameter plays a role in preventing overfitting. The score increases as increasing the number of max_depth , while the gap between the scores of training and the test becomes large. Figure 3 (d) shows the importance of each feature. The integrated intensity of $C^{18}O$ plays a significant role in predicting the H_2 column density. The integrated intensity of ^{12}CO and ^{13}CO

¹ The validation curve plot only displays numbers up to 1 less than the max_depth value is due to the implementation of the function used to create the validation curve plot. In the case of $\text{max_depth}=11$, the validation curve function tries max_depth values from 1 to 10 and plots the cross-validation results.

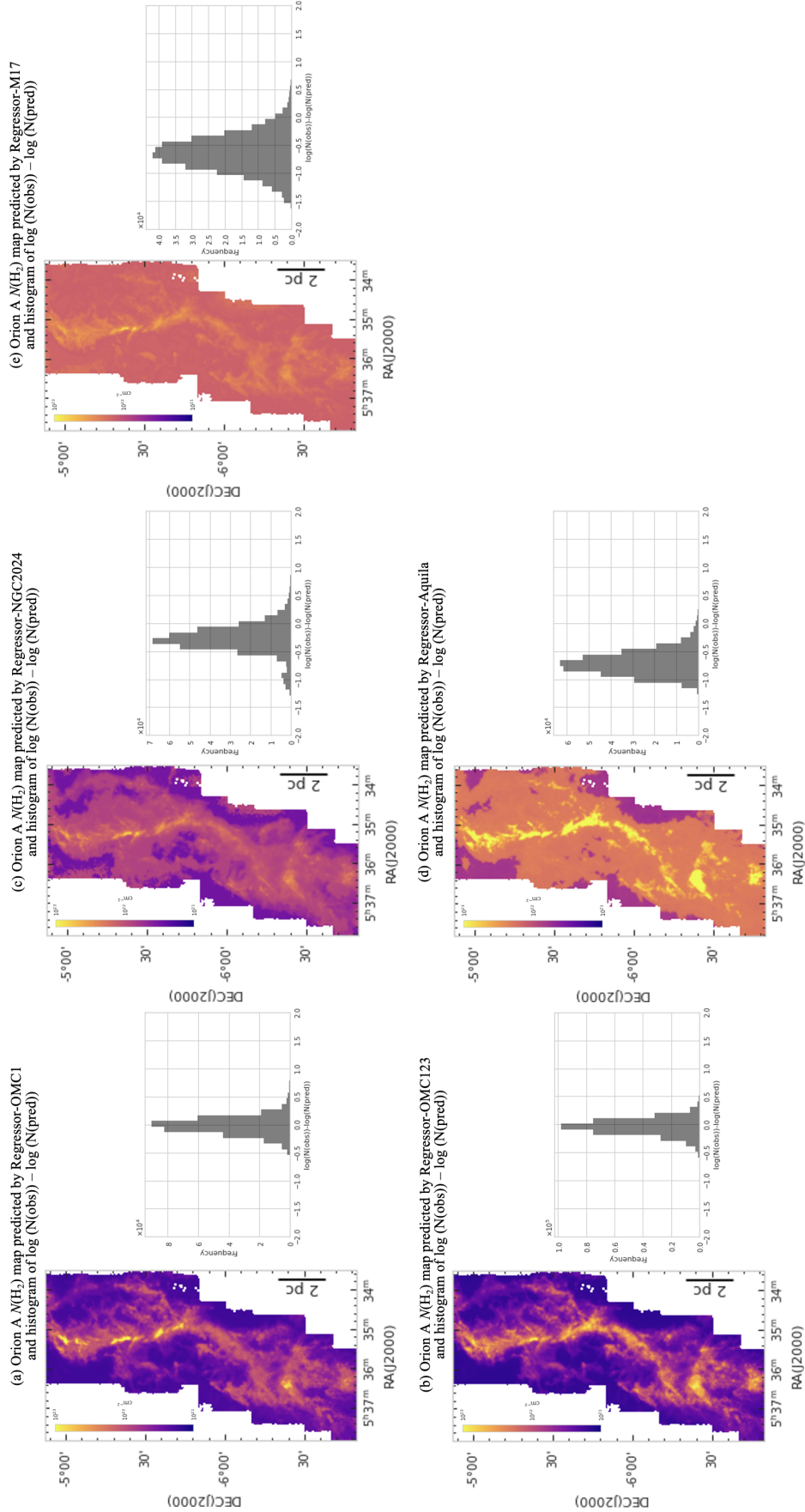


Figure 5. Comparison of the predicted H_2 column density maps toward Orion A predicted by using (a) Regressor-OMC1, (b) Regressor-OMC123, (c) Regressor-NGC2024, (d) Regressor-Aquila, and (e) Regressor-M17 and histograms of $\log(N(\text{obs})) - \log(N(\text{pred}))$.
MNRAS **000**, 1–14 (2015)

also plays a role. In the case of Regressor-OMC1, the sum of the importance values for ^{12}CO , ^{13}CO , and C^{18}O integrated intensity maps is ~ 0.75 , while the sum for all features is 1.0. Although the fraction of the importance values for other features is smaller than those for the integrated intensity maps, other features also play a role in the prediction. Table 3 summarizes the parameters tuned for the given data set ².

4 RESULTS

4.1 Distribution of the predicted H_2 column density

4.1.1 Orion A

Figure 2 compares the predicted and observed H_2 column density maps of Orion A. While only a small portion of the CO maps of the Orion A region, that with the highest H_2 column density (marked by a black rectangle), was used for training the regressor, the predicted H_2 column density map is quite similar to the reference H_2 column density map in most of the region.

Figure A1 shows the results when the data around a larger area encompassing OMC-1/2/3 regions is used for the training. While the overall distribution of the predicted H_2 column density is similar to that of the observed H_2 column density, the prediction at higher H_2 column density is overestimated.

Figure 4(a) shows the pixel-to-pixel correlation between the observed H_2 column density and H_2 column density predicted by Regressor-OMC1. The predicted H_2 column density is mostly the same as the observed H_2 column density. For the observed H_2 column densities $< 2 \times 10^{21} \text{ cm}^{-2}$, the scatter of the predicted H_2 column densities is slightly larger than for the larger H_2 column density values because of the noise present in the molecular line data.

Figure 4(b) shows the pixel-by-pixel histogram of the observed H_2 column density and the H_2 column density predicted by Regressor-OMC1 toward the whole Orion A region. The H_2 column density less than 10^{21} cm^{-2} is not predicted well by the regressor.

Figure 4(c) shows the pixel-by-pixel histogram of the observed H_2 column density and the H_2 column density predicted by Model-OMC1 toward the area that is used for the training in Model-OMC1. The overall distribution between the observed and predicted H_2 column density is similar.

Figure 4(d) shows the pixel-by-pixel histogram of the observed H_2 column density and the H_2 column density predicted by Regressor-OMC1 toward the area that is not used for the training in Regressor-OMC1. The column densities of $< 10^{21} \text{ cm}^{-2}$ and $> 5 \times 10^{22} \text{ cm}^{-2}$ are not well predicted. These suggest that the prediction accuracy at the column densities of $< 10^{21} \text{ cm}^{-2}$ and $> 5 \times 10^{22} \text{ cm}^{-2}$ is low. The reason why the column densities of $< 10^{21} \text{ cm}^{-2}$ is not well predicted is that the training area does not contain low column density samples. The reason why the column densities of $> 5 \times 10^{22} \text{ cm}^{-2}$ is not well predicted is discussed in Sect. 5.2.

Figure 5 (a) shows the predicted H_2 column density maps toward Orion A predicted by using Regressor-OMC1 and histograms of $\log(N(\text{obs})) - \log(N(\text{pred}))$. The residual of $\log(N(\text{obs})) - \log(N(\text{pred}))$ shows the Gaussian distribution with a center of $\log(N(\text{obs})) - \log(N(\text{pred})) = 0$, suggesting the model makes a good prediction.

² The best hyperparameters evaluate the performance of the model by trying combinations of hyperparameters. The model's performance is averaged over multiple training and evaluation runs using cross-validation.

4.1.2 Orion B/NGC 2024, Aquila, and M 17

We also made regressors using a small portion of the Orion B/NGC 2024, Aquila, and M 17 maps, respectively, and applied them to predict the H_2 column density toward the whole map. Figures A2, A3, and A4 compare the predicted and observed H_2 column density maps toward Orion B/NGC 2024, Aquila, and M 17. The overall distributions of the predicted H_2 column density in each region are similar to those of the observed H_2 column density. It is also worth mentioning that two condensations associated with the young stellar objects seen in the HGBS H_2 column density map are not seen in the predicted H_2 column density map of NGC 2024 (see magenta open circles in Fig. A2). This implies that the conversion factor from the CO and its isotope's intensities to the H_2 column density are completely different (i.e., the relation between H_2 column density and molecular intensities around these two condensations is different compared with the overall environment). This also may suggest that the prediction of the H_2 column density by machine learning is helpful in finding regions of the cloud with atypical gas properties.

5 DISCUSSION

5.1 Comparison between the observed and predicted H_2 column density maps

Table 5 summarizes the predicted total H_2 column density fraction to the observed total H_2 column density. The predicted total column density, $N(\text{pred})_{\text{tot}}$, is derived using the equation $N(\text{pred})_{\text{tot}} = \sum N(\text{pred})$, where $N(\text{pred})$ is the predicted column density at each pixel. The observed total column density, $N(\text{obs})_{\text{tot}}$, is derived using the equation $N(\text{obs})_{\text{tot}} = \sum N(\text{obs})$, where $N(\text{obs})$ is the observed column density at each pixel. The mass of each cloud, M_{cloud} is estimated as

$$M_{\text{cloud}} = AN_{\text{tot}}m_{\text{H}}\mu_{\text{H}_2}, \quad (9)$$

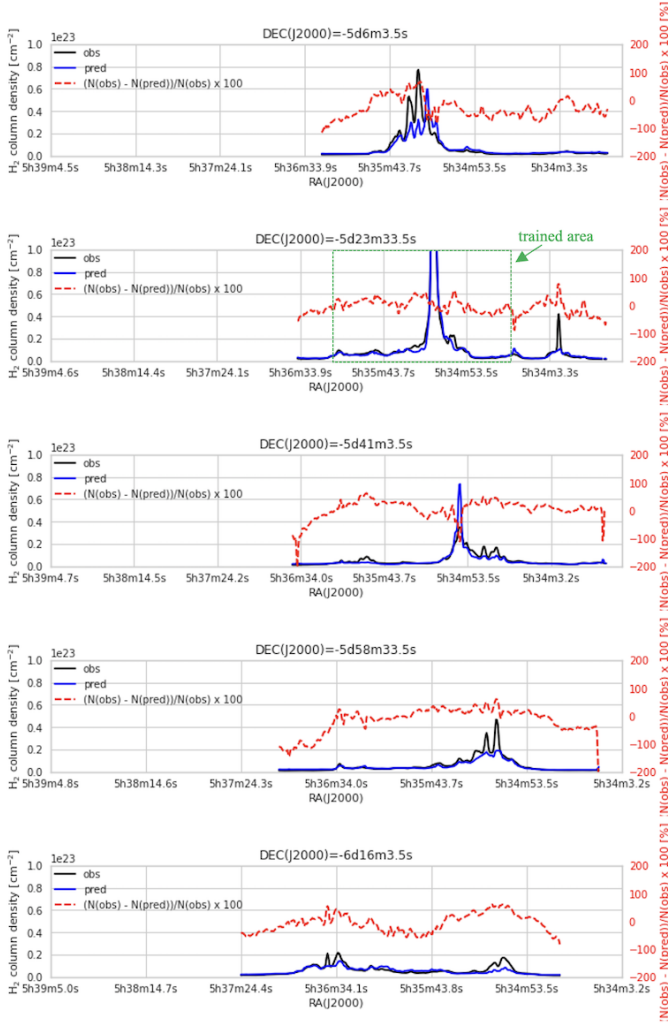
,where A is the surface area, m_{H} is the hydrogen atom mass, and $\mu_{\text{H}_2} = 2.8$ is the mean molecular weight per H_2 molecule (Shimajiri et al. 2017). Thus, on the comparison toward the same area, the relation between $N(\text{pred})_{\text{tot}}$ and $N(\text{obs})_{\text{tot}}$ is proportional to the relation between the predicted mass and observed mass. If the area used for the training is inside the area where the H_2 column density is predicted, the fraction ranges from 95% to 109%. However, if the area used for the training is not inside the area where the H_2 column density is predicted, significant variations in the fraction are seen. This indicates that variations in the molecular abundance among clouds are not corrected. However, the H_2 column density in Orion B/NGC 2024 predicted by Regressor-NGC2024, Regressor-OMC1, and Regressor-OMC123 is relatively similar (95%, 133%, and 126%), suggesting similar gas properties/abundance in these clouds.

This analysis suggests that H_2 column densities can be well reconstructed using machine learning when the training data sets have similar properties as those of the clouds for which the H_2 column density is reconstructed. In the case where the training sets and the studied clouds have different gas properties, the machine learning method is not optimum. This can be improved by increasing the number of clouds with different properties in the training step and the molecular species used for the training.

Here, we also compared the fraction of the predicted total H_2 column density to the observed total H_2 column density

Table 5. Fraction of predicted to observed total $N(\text{H}_2)$ column density in the case of Regressor-OMC1

		Regressor				
		Regressor-OMC1	Regressor-OMC123	Regressor-NGC2024	Regressor-Aquila	Regressor-M17
Predicted Area	Orion A	97%	109%	134%	393%	278%
	Orion B/NGC 2024	133%	126%	95%	263%	266%
	Aquila	80%	113%	86%	102%	206%
	M 17	160%	153%	75%	260%	101%

**Figure 6.** Profiles of the H_2 column density along the RA direction. The Dec of cut lines is indicated at the top of each panel. The black and blue curves indicate the profiles of the observed and predicted H_2 column density ($N(\text{obs})$ and $N(\text{pred})$). The red curve indicate fraction of $N(\text{obs}) - N(\text{pred})/N(\text{obs}) \times 100$. The green box indicates the area that is used for training.

$(N(\text{pred})_{\text{tot}}/N(\text{obs})_{\text{tot}})$ with that of the total H_2 column density derived from ^{12}CO (1–0) integrated intensity using X_{CO} factor to the observed total H_2 column density ($N(X_{\text{CO}})_{\text{tot}}/N(\text{obs})_{\text{tot}}$). As summarized in Table 6, the fraction of $N(X_{\text{CO}})_{\text{tot}}/N(\text{obs})_{\text{tot}}$ varies from 70% to 257%, while the fraction of $N(\text{pred})_{\text{tot}}/N(\text{obs})_{\text{tot}}$ varies from 95% to 110%. This comparison suggests that the Machine learning

technique provides the total cloud mass with a smaller uncertainty than the total cloud mass estimate using X_{CO} .

5.2 Comparison of the observed and predicted H_2 column density profiles across the maps

As described in Sect. 4.1.1, there is a trend that the accuracy of predicting H_2 column density is lower at higher H_2 column density. To investigate which portion of the cloud structures is lower accuracy in the predicted H_2 column density, we produced profiles along the RA direction as shown in Fig. 6. The distributions of the profile at H_2 column density $N(\text{H}_2) < \sim 1 \times 10^{22} \text{ cm}^{-2}$ are similar between the predicted and observed H_2 column density, while the peaks with H_2 column density $N(\text{H}_2) > \sim 2 \times 10^{22} \text{ cm}^{-2}$ is not predicted well. These peaks correspond to the dense star-forming gas often organized in filamentary structures. The reason why the higher H_2 column density is not predicted well is that the ^{12}CO , ^{13}CO , and C^{18}O used in training do not trace well the dense gas (Shimajiri et al. 2015a). Thus, to predict the higher H_2 column density, dense gas tracers such as H^{13}CO^+ and N_2H^+ are required. Shimajiri et al. (2017) reported that the H^{13}CO^+ (1–0) emission traces HGBS filaments very well above $A_V > 16$. The results by Gratier et al. (2021) support our results (also see Sect. 1).

5.3 Application of trained regressors to other clouds

To investigate whether we can predict the H_2 column density for different clouds from those in which they were trained, we applied each model to the data set of all other clouds. As shown in Fig. 5, the distributions of the predicted H_2 column density of each cloud are not the same when different training sets are used. The fraction of the H_2 column density predicted by each model to the observed H_2 column density in each cloud is listed in Table 5. When the Regressor-OMC1 is applied to the data set of Orion B/NGC 2024, Aquila, and M 17, the fractions of the predicted H_2 column density to the observed H_2 column density are 133%, 80%, and 160%, respectively (column Regressor-OMC1 in Table 5). When the Regressor-OMC123 is applied to the data set of Orion B/NGC 2024, Aquila, and M 17, the fractions are 126%, 113%, and 153%, respectively (column Regressor-OMC123 in Table 5). When the Regressor-NGC2024 is applied to the data set of Orion A, Aquila, and M 17, the fractions are 134%, 86%, and 75%, respectively (column Regressor-NGC2024 in Table 5). When the Regressor-Aquila is applied to the data set of Orion A, Orion B/NGC 2024, and M 17, the fractions of the predicted H_2 column density to the observed H_2 column density are 393%, 263%, and 260%, respectively (column Regressor-Aquila in Table 5). One of the problems of Aquila is that the background in the dust continuum is very strong (Könyves et al. 2015), thus not all the column density derived from *Herschel* comes from the cloud emission but is rather a result of the line of sight integration. That may be a reason for this overestimation. When the Regressor-M 17 is applied to

Table 6. Comparison of predicted, observed, and X_{CO} -derived total H_2 column densities across entire fields

Predicted Area	Orion A		NGC 2024	Aquila	M 17
Regressor	Regressor-OMC1	Regressor-OMC123	Regressor-NGC2024	Regressor-Aquila	Regressor-M17
$N(\text{pred})_{\text{tot}}^\dagger/N(\text{obs})_{\text{tot}}^\ddagger$	97%	109%	95%	102%	101%
$N(X_{CO})_{\text{tot}}^\bullet/N(\text{obs})_{\text{tot}}^\ddagger$	257%	257%	394%	70%	222%

† : $N(\text{pred})_{\text{tot}}$ is the predicted total column density. $N(\text{pred})_{\text{tot}} = \sum N(\text{pred})$, where $N(\text{pred})$ is the predicted column density at each pixel.

‡ : $N(\text{obs})_{\text{tot}}$ is the observed total column density. $N(\text{obs})_{\text{tot}} = \sum N(\text{obs})$, where $N(\text{obs})$ is the observed column density at each pixel.

$^\bullet$: $N(X_{CO})_{\text{tot}}$ is the X_{CO} -derived total column density. $N(X_{CO})_{\text{tot}} = \sum N(X_{CO})$, where $N(X_{CO})$ is the X_{CO} -derived column density at each pixel.

the data set of Orion A, Orion B/NGC 2024, and Aquila, the fractions are 278%, 266%, and 206%, respectively (column Regressor-M17 in Table 5). The large variations in the fraction (75–393%) are recognized. However, the fractions in the cases where the regressor trained in Orion A (OMC-1 and OMC-123) applied to Orion B/NGC 2024 and the regressor trained in Orion B/NGC 2024 applied to Orion A tend to be smaller (95–134%). These results indicate that the abundances of the molecule used in this study vary among the clouds and the current method using machine learning could not correct these variations. Orion A and Orion B are in the same giant molecular cloud complex. Thus, similar abundances in Orion A and Orion B are expected compared with those in other clouds. To test this hypothesis, we made a regressor trained in Orion A, Aquila, and M 17, then applied the model to NGC 2024. But, the fraction and distribution of the predicted H_2 column density were not improved. Training in more clouds might be required to correct the abundance variations among clouds and also using more molecular species tracing different densities and different environments.

5.4 Predicting $N(H_2)$ map with higher-angular resolution

In Section 4, we trained and created regressors by adjusting H_2 column densities in a small portion of each cloud where both molecular line data and *Herschel* data were available. Then, a H_2 column density map for an area much wider than that used for training was predicted from the molecular line data by applying the trained regressor. This indicates that our method can successfully predict the H_2 column density in an area not observed by *Herschel* and can also generate H_2 column density maps at higher angular resolution if *Herschel* column density data are available for a small portion of a given field and molecular line data exist for a larger area.

Schuller et al. (2021) observed the northern part of the Orion A molecular cloud, which covers the OMC-1, OMC-2, and OMC-3 regions with the ArTéMiS³ camera (see André et al. 2016) installed on the Atacama Pathfinder EXperiment (APEX) telescope and produced a H_2 column density map of the integral-shaped filament at 8'' resolution. Kong et al. (2018) obtained ^{12}CO (1–0), ^{13}CO (1–0), and C^{18}O (1–0) maps of the Orion A cloud at 8'' resolution, which cover a larger area than the ArTéMiS camera map, by combining ^{12}CO (1–0), ^{13}CO (1–0), and C^{18}O (1–0) data from the Nobeyama 45m telescope with interferometric data from the Combined Array for Research in Millimeter-wave Astronomy (CARMA).

First, we generated a $N(H_2)$ predictor (Regressor-High-Resolution) by training the regressor over the entire area mapped with ArTéMiS. We then used this regressor to predict H_2 column

density values in areas observed with CARMA but not covered by ArTéMiS, resulting in a wide-field, 8'' resolution $N(H_2)$ map. Figure 7 shows the ArTéMiS+*Herschel* 8'' resolution $N(H_2)$, the predicted 8'' resolution $N(H_2)$, the fidelity maps, and the fidelity histogram. The pixels covering the lower column density are limited on the ArTéMiS+*Herschel* 8'' resolution $N(H_2)$ map. In other words, the training is insufficient at low column densities. This causes an overestimation of the predicted H_2 column density at low column densities (see Figure 7 (d)). However, the overall distribution of the integral-shape filament is well predicted (Figure 7 (c)).

To evaluate whether the 8'' angular resolution $N(H_2)$ map is predicted well, we compared the predicted H_2 column density map smoothed to 18''.2 from 8'' with the 18''.2 resolution *Herschel* H_2 column density map. Figure 8 shows the pixel-to-pixel correlation between the predicted and observed H_2 column densities on the 18''.2 resolution and their histograms. The overall distribution is in good agreement, although the predicted H_2 column density in the trained and non-trained areas tends to be 10% and 40% larger than the observed H_2 column density, respectively (see Fig. 8(a)). In particular, for $N(H_2) < 2 \times 10^{21} \text{ cm}^{-2}$, the predicted H_2 column density is almost an order of magnitude larger than the observed H_2 column density. The reason is that the area of $N(H_2) < 2 \times 10^{21} \text{ cm}^{-2}$ is not trained (see red points in Fig. 8(a)), and the Regressor-High-Resolution cannot accurately predict the H_2 column density of $N(H_2) < 2 \times 10^{21} \text{ cm}^{-2}$.

As discussed above, the machine-learning predictions of H_2 column density made in this study allow us to do the following: (1) extend the coverage of the H_2 column density maps obtained with the *Herschel* space observatory by using ground-based data, and (2) enable the production of H_2 column density maps with an angular resolution higher than 18''.2, which could not be obtained only with the *Herschel* telescope, from the molecular line data obtained with interferometers such as CARMA and ALMA⁴.

6 CONCLUSIONS

To investigate the potential of machine learning in producing reliable H_2 column density maps, we generated a number of H_2 column density maps from ^{12}CO (1–0), ^{13}CO (1–0), and C^{18}O (1–0) data using the python package *pycaret*. Our main results can be summarized as follows:

(i) For the given data set, the model of the Extra Trees Regressor (ET) showed the best score in MAE, MSE, RMSE, RMSLE, and MAPE, although the training time tends to be longer than other models. In this study, we used the ET model.

³ See <https://www.apex-telescope.org/ns/artemis/>

ArTéMiS stands for “ARchitectures de bolomètres pour des Telescopes à grand champ de vue dans le domaine sub-Millimétrique au Sol” in French.

⁴ ALMA stands for the Atacama Large Millimeter/submillimeter Array

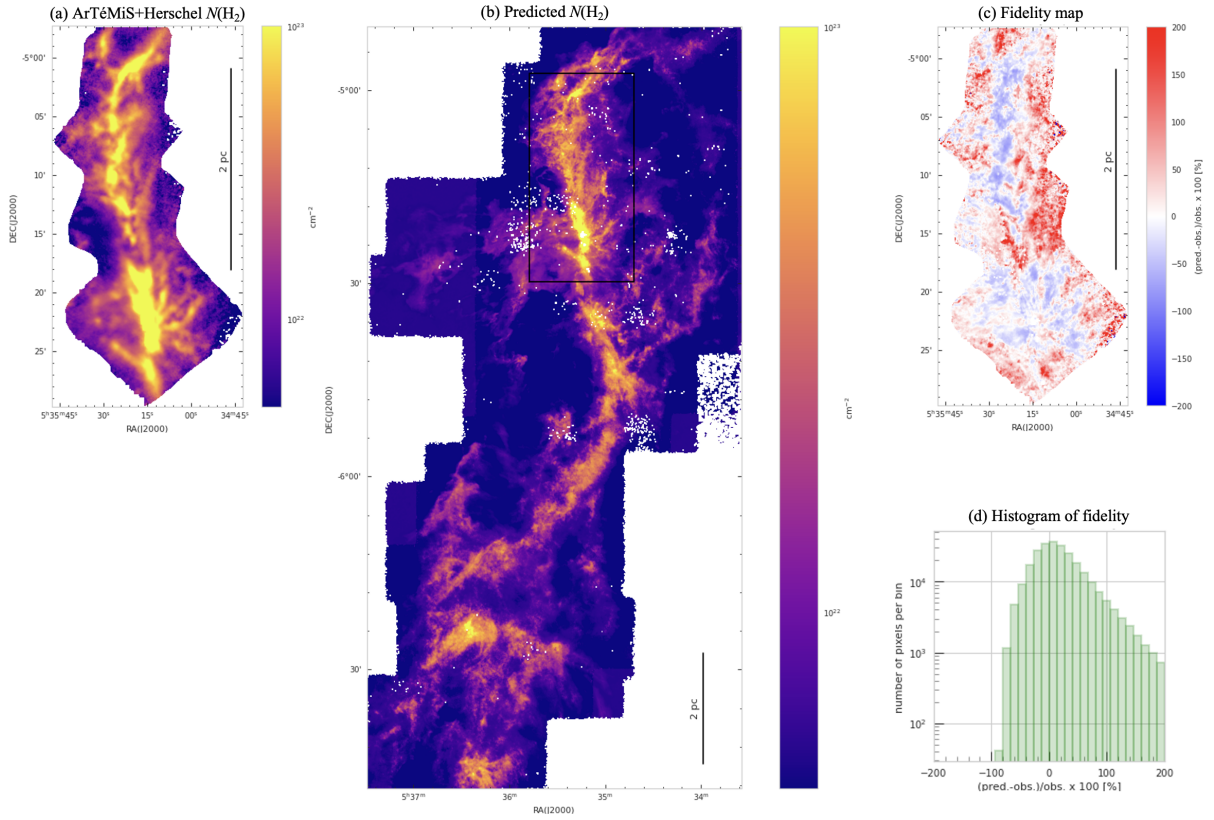


Figure 7. Same as Figure 2, but predicted by Regressor-High-Resolution. The displayed area in panels (a) and (c) corresponds to the area indicated by the black box in panel (b).

(ii) The overall distribution of the predicted H_2 column density is similar to that of *Herschel*-derived column density maps. The predicted total H_2 column density is also consistent within 10% compared with the observed total H_2 column density when we created the model by training the small portion of the trained area in the same cloud. The ratio of the predicted H_2 column density to the observed H_2 column density ranges from 95% to 110%, while the ratio of the H_2 column density derived using the X_{CO} factor to the observed H_2 column density ranges from 70% to 257%.

(iii) Comparing the predicted and observed H_2 column density maps in NGC 2024, we found that two condensations associated with the young stellar objects seen in the HGBS H_2 column density map are not seen in the predicted H_2 column density map. This implies that the conversion factor from the CO and its isotope’s intensities to the H_2 column density are completely different (i.e., the relation between H_2 column density and molecular intensities is different). This also may suggest that the prediction of the H_2 column density by machine learning is helpful in finding such unique regions in the clouds.

(iv) We also investigated whether we can predict the H_2 column density for clouds different from those in which they were trained. Do to so, we applied each data set model to all the other clouds. We found that the H_2 column density is not predicted well by using the model trained in the data set of another cloud, suggesting that the abundances of the molecule used in this study vary among the clouds and the machine learning could not correct these variations.

(v) We succeed in producing an $8''$ resolution $N(\text{H}_2)$ map from the ^{12}CO , ^{13}CO , and C^{18}O (1–0) line data obtained with CARMA and the Nobeyama 45m telescope. This indicates that the machine-

learning technique in this study allows us to extend the H_2 column densities map obtained with the *Herschel* Space Observatory by using ground-based radio telescopes and to produce a H_2 column density map with an angular resolution higher than $18''.2$, which could not be obtained only with the *Herschel* telescope, from the molecular line data obtained with interferometers.

ACKNOWLEDGEMENTS

We thank the referee for useful suggestions that improved the clarity of the paper. This work was supported by JSPS KAKENHI Grant Numbers JP19K23463, JP20K04035, and JP21H00057. This work was also supported by “Young interdisciplinary collaboration project” in the National Institutes of Natural Sciences (NINS). This work was supported (in part) by a University Research Support Grant from the National Astronomical Observatory of Japan (NAOJ). This research has made use of data from the HGBS and HOBYS projects. The authors are grateful to Kaoru NISHIKAWA and Daisuke YOSHIDA for the useful discussion.

DATA AVAILABILITY

The data underlying this article are available in the article.

REFERENCES

André P., et al., 2010, *A&A*, **518**, L102

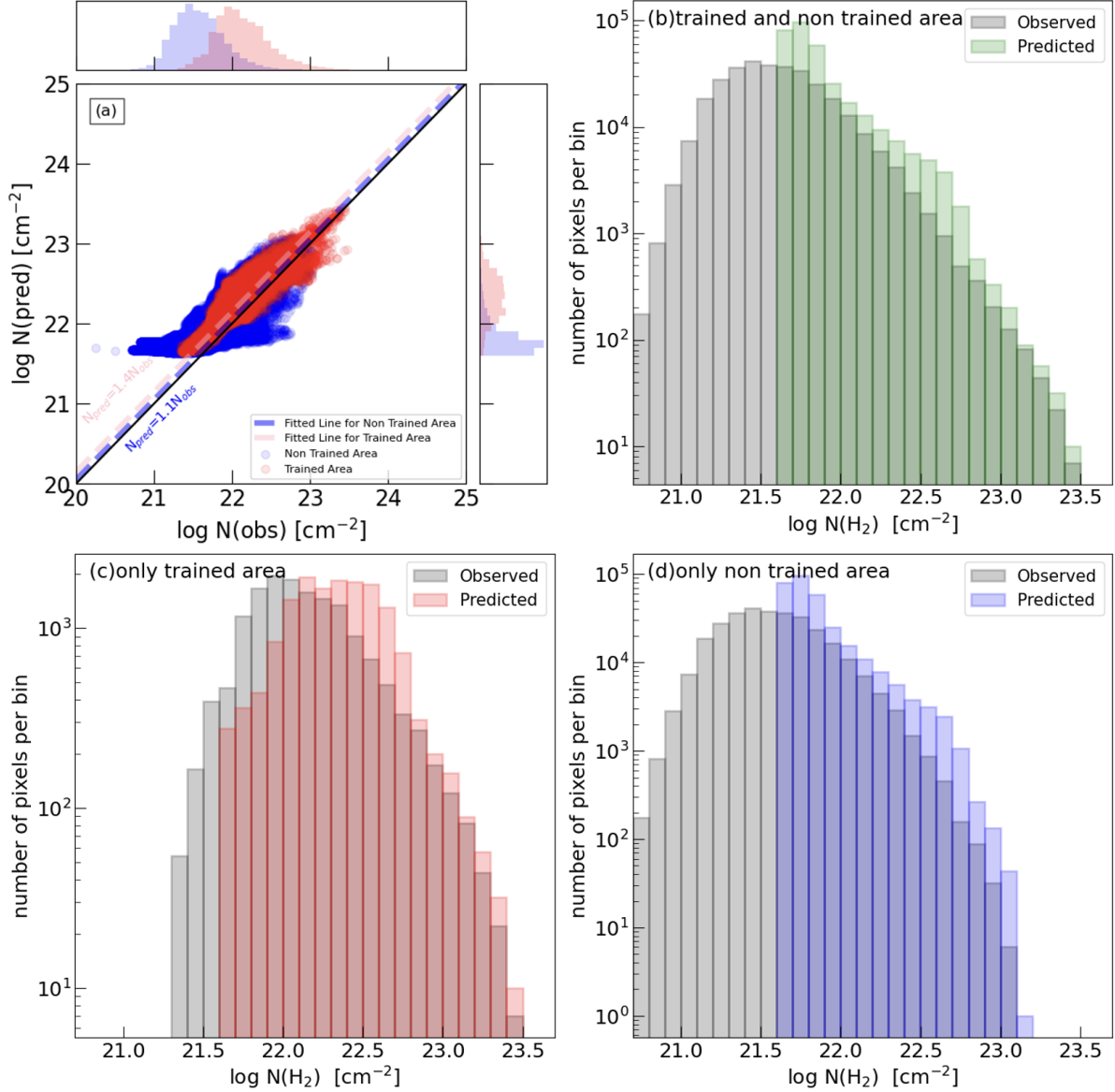


Figure 8. (a) Pixel-to-pixel correlation between predicted and observed H_2 column density on the 18"2 resolution and (b) pixel-by-pixel H_2 column density histogram for predicted and observed H_2 column density in the whole Orion A region, (c) pixel-by-pixel H_2 column density histogram for predicted and observed H_2 column density in the area trained for Regressor-High-Resolution (i.e., inside of the black box in Fig. 7 (a)), and (d) pixel-by-pixel H_2 column density histogram for predicted and observed H_2 column density in the area not used for Regressor-High-Resolution (i.e., outside of the black box in Fig. 7 (a)). In panel (a), the black line indicates the predicted H_2 column density equals the observed H_2 column density. In panel (a), the red and blue dashed lines indicate the best fits results for the trained area and non-trained area: $N_{\text{pred}} = 1.4 \times N_{\text{obs}}$ and $N_{\text{pred}} = 1.1 \times N_{\text{obs}}$. The top and right on the panel (a) show the histograms of $\log N(\text{obs})$ and $\log N(\text{pred})$ for the non-trained area and trained area, respectively. In panel (b-d), the red, green, and blue indicate the predicted H_2 column density, while the gray indicates the observed H_2 column density.

André P., et al., 2016, *A&A*, 592, A54
 Barchi P. H., et al., 2020, *Astronomy and Computing*, 30, 100334
 Bolatto A. D., Wolfire M., Leroy A. K., 2013, *ARA&A*, 51, 207
 Braiding C., et al., 2018, *Publ. Astron. Soc. Australia*, 35, e029
 Fujita S., et al., 2022, *arXiv e-prints*, p. arXiv:2212.06238
 Geurts P., Ernst D., Wehenkel L., 2006, *Machine Learning*, 63, 3
 Gratier P., et al., 2021, *A&A*, 645, A27
 Ishii S., Nakamura F., Shimajiri Y., Kawabe R., Tsukagoshi T., Dobashi K., Shimoikura T., 2019, *PASJ*, 71, S9
 Kong S., et al., 2018, *ApJS*, 236, 25
 Könyves V., et al., 2015, *A&A*, 584, A91
 Könyves V., et al., 2020, *A&A*, 635, A34

Lin S.-J., et al., 2016, *ApJ*, 826, 193
 Mangum J. G., Shirley Y. L., 2015, *PASP*, 127, 266
 Motte F., et al., 2010, *A&A*, 518, L77
 Nakamura F., et al., 2019, *PASJ*, 71, S3
 Nishimoto S., et al., 2022, in *Society of Photo-Optical Instrumentation Engineers (SPIE) Conference Series*. p. 121891Q, doi:10.1117/12.2628664
 Nishimura A., et al., 2015, *ApJS*, 216, 18
 Nishimura Y., Shimonishi T., Watanabe Y., Sakai N., Aikawa Y., Kawamura A., Yamamoto S., 2016, *ApJ*, 829, 94
 Palmeirim P., et al., 2013, *A&A*, 550, A38
 Roy A., et al., 2014, *A&A*, 562, A138
 Schanche N., et al., 2019, *MNRAS*, 483, 5534

- Schuller F., et al., 2021, *A&A*, 651, A36
- Shimajiri Y., et al., 2011, *PASJ*, 63, 105
- Shimajiri Y., et al., 2014, *A&A*, 564, A68
- Shimajiri Y., et al., 2015a, *ApJS*, 217, 7
- Shimajiri Y., et al., 2015b, *ApJS*, 221, 31
- Shimajiri Y., et al., 2017, *A&A*, 604, A74
- Shimajiri Y., André P., Peretto N., Arzoumanian D., Ntormousi E., Könyves V., 2023, *A&A*, 672, A133
- Shimoikura T., Dobashi K., Nakamura F., Shimajiri Y., Sugitani K., 2019a, *PASJ*, 71, S4
- Shimoikura T., Dobashi K., Hirose A., Nakamura F., Shimajiri Y., Sugitani K., 2019b, *PASJ*, 71, S6
- Su Y., et al., 2019, *ApJS*, 240, 9
- Sugitani K., et al., 2019, *PASJ*, 71, S7
- Tokuda K., et al., 2021, *ApJ*, 922, 171
- Torii K., et al., 2019, *PASJ*, 71, S2
- Ueda S., et al., 2020, in Society of Photo-Optical Instrumentation Engineers (SPIE) Conference Series. p. 114522L, doi:10.1117/12.2560830
- Umemoto T., et al., 2017, *PASJ*, 69, 78
- Watanabe Y., Sakai N., Sorai K., Yamamoto S., 2014, *ApJ*, 788, 4
- Watanabe Y., Nishimura Y., Sorai K., Sakai N., Kuno N., Yamamoto S., 2019, *ApJS*, 242, 26
- Zavagno A., et al., 2023, *A&A*, 669, A120

APPENDIX A: SOME EXTRA MATERIAL

Figure A1 compares the predicted and observed H₂ column density maps of Orion A. For the training, the data around an area encompassing OMC-1/2/3 regions is used. Figure A2 compares the predicted and observed H₂ column density maps of Orion B/NGC 2024. The column density is predicted by Regressor-NGC202. Figure A3 compares the predicted and observed H₂ column density maps of Aquila. The column density is predicted by Regressor-Aquila. Figure A4 compares the predicted and observed H₂ column density maps of M 17. The column density is predicted by Regressor-M17.

This paper has been typeset from a $\text{\TeX}/\text{\LaTeX}$ file prepared by the author.

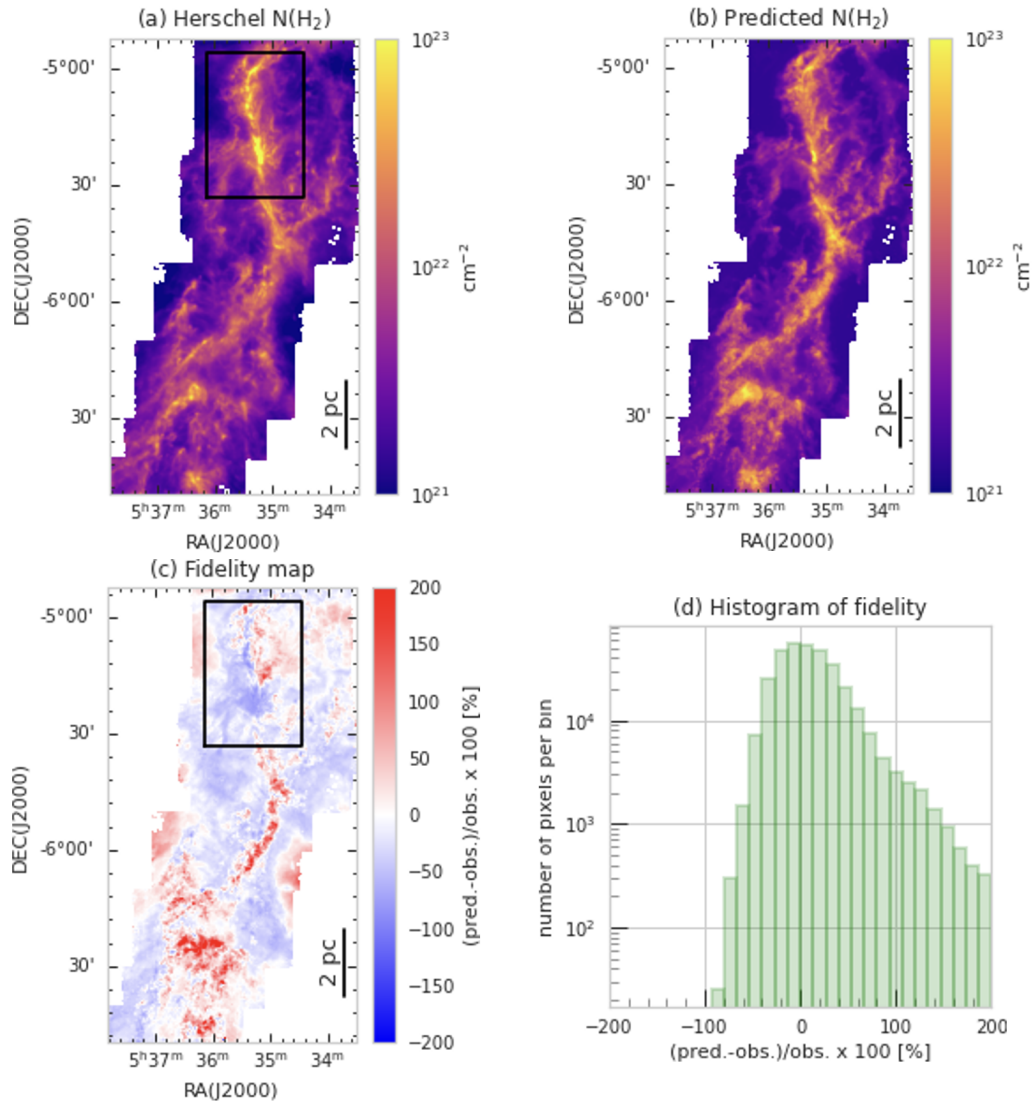


Figure A1. Same as Figure 2, but predicted by Regressor-OMC123.

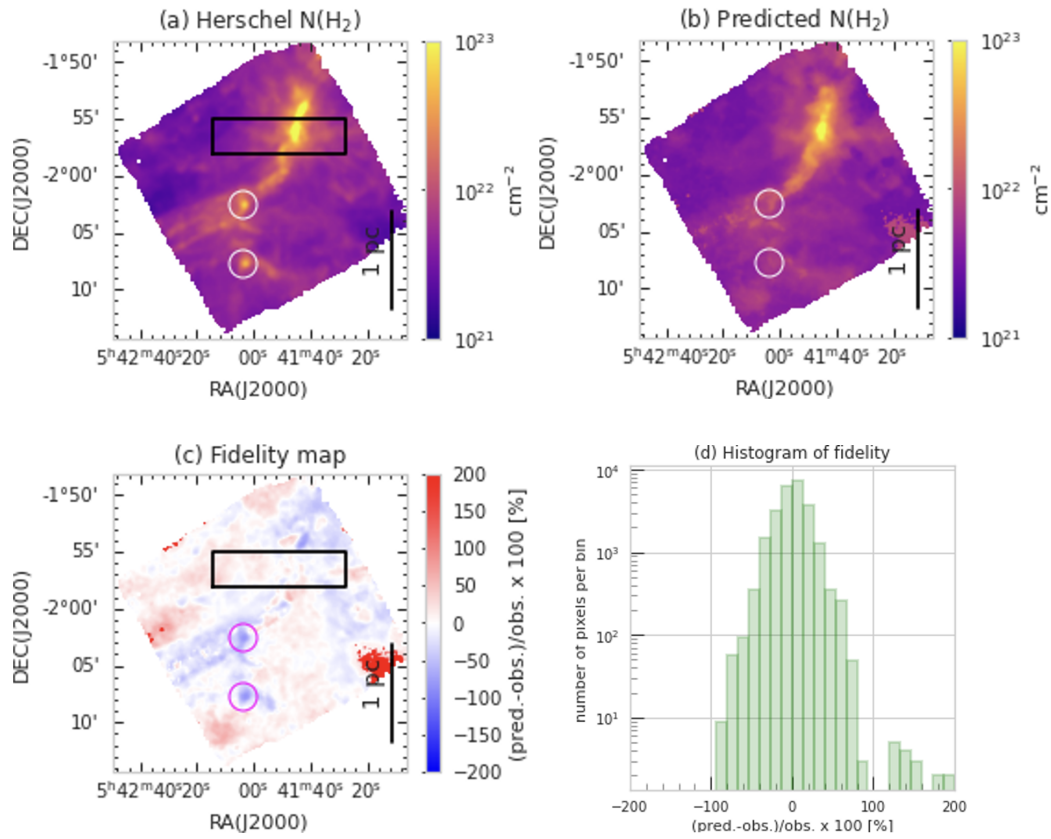


Figure A2. Same as Figure 2, but toward Orion B/NGC 2024 and predicted by Regressor-NGC2024. The white open circles indicate the location of two condensations seen in the observed H₂ column density map and not in the predicted H₂ column density map.

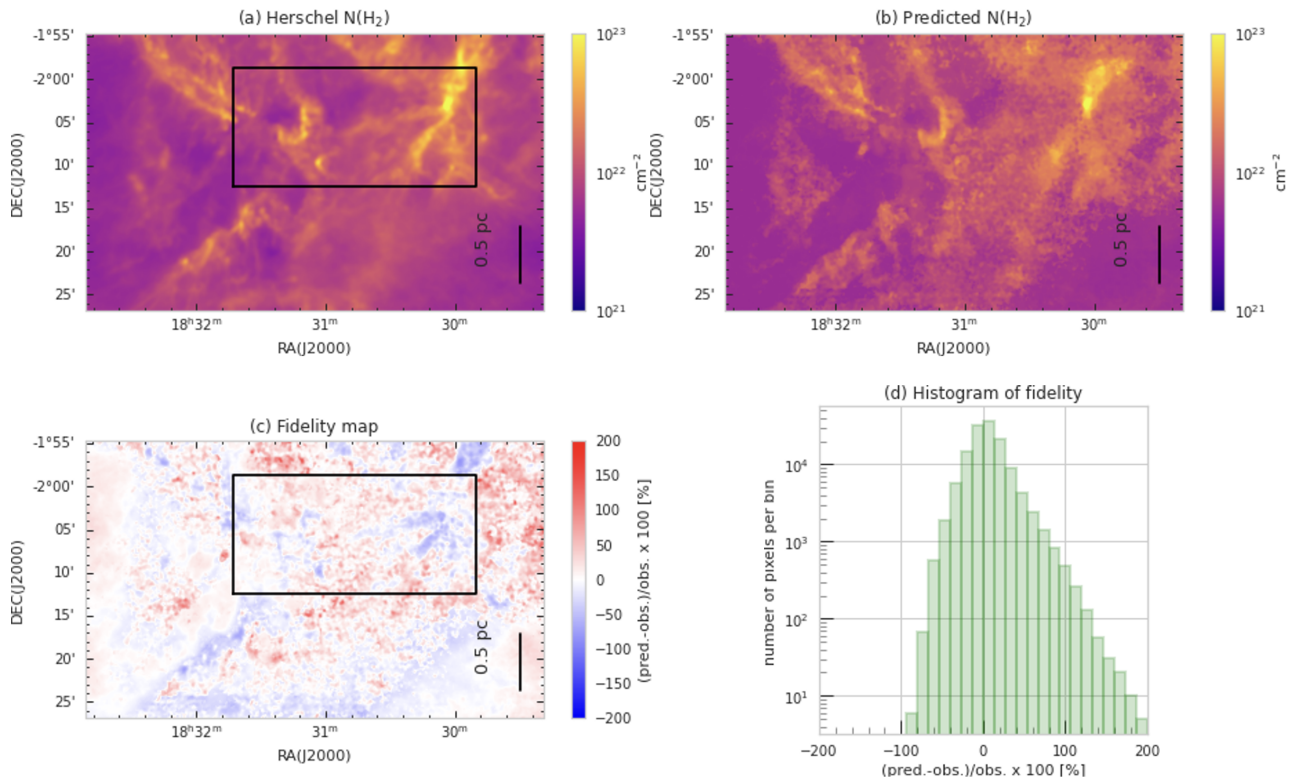


Figure A3. Same as Figure 2, but toward Aquila and predicted by Regressor-Aquila.

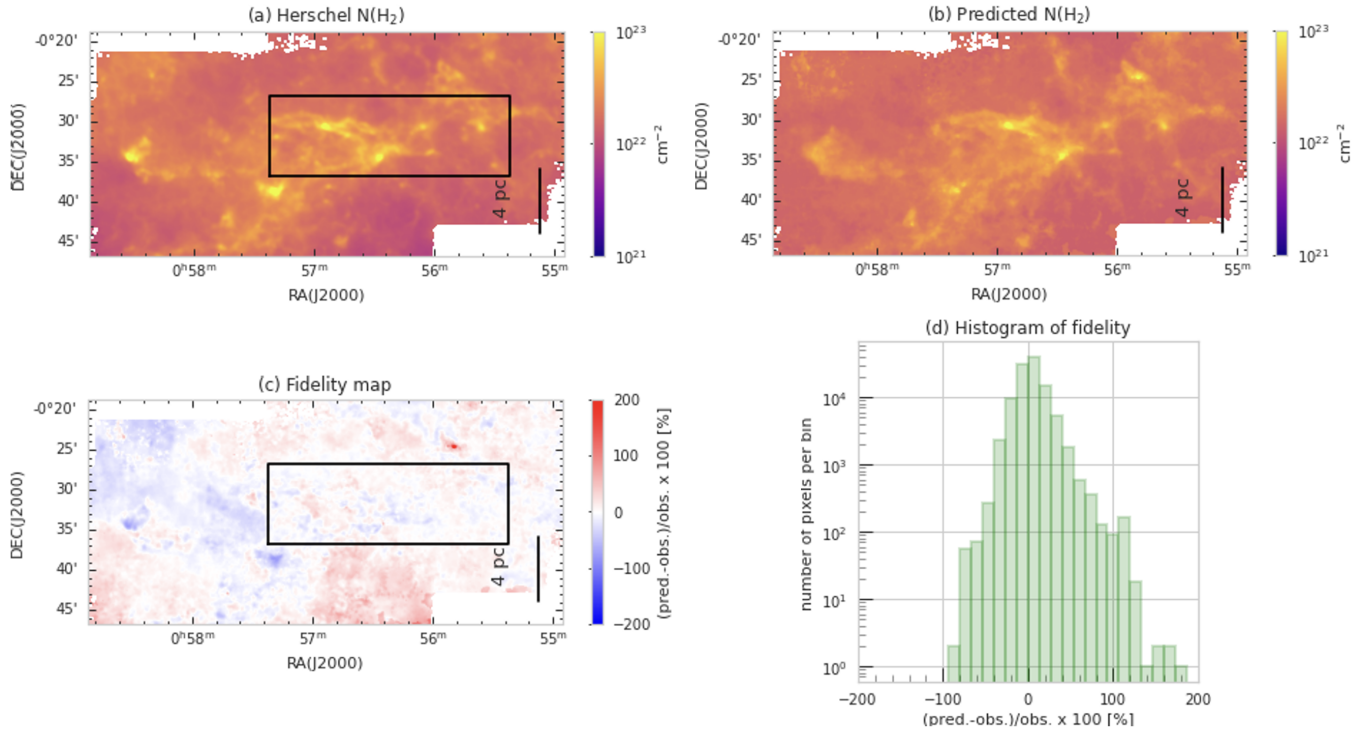


Figure A4. Same as Figure 2, but toward M 17 and predicted by Regressor-M17.